Article

Fracture Toughness Prediction under Compressive Residual Stress by Using a Stress-Distribution T-Scaling Method

Toshiyuki Meshii [1],* (ID) **and Kenichi Ishihara [2]** (ID)

1   Faculty of Engineering, University of Fukui, Fukui 910-8507, Japan
2   Kobelco Research Institute, Inc. 1-5-5 Takatsukadai, Nishi-ku, Kobe, Hyogo 651-2271, Japan;
     ishihara.kenichi@kki.kobelco.com
*   Correspondence: meshii@u-fukui.ac.jp; Tel.: +81-776-27-8468

Abstract: The improvement in the fracture toughness J_c of a material in the ductile-to-brittle transition temperature region due to compressive residual stress (CRS) was considered in this study. A straightforward fracture prediction was performed for a specimen with mechanical CRS by using the T-scaling method, which was originally proposed to scale the fracture stress distributions between different temperatures. The method was validated for a 780-MPa-class high-strength steel and 0.45% carbon steel. The results showed that the scaled stress distributions at fracture loads without and with CRS are the same, and that J_c improvement was caused by the loss in the one-to-one correspondence between J and the crack-tip stress distribution. The proposed method is advantageous in possibly predicting fracture loads for specimens with CRS by using only the stress–strain relationship, and by performing elastic-plastic finite element analysis, i.e., without performing fracture toughness testing on specimens without CRS.

1. Introduction

It is well known that some types of preloading improve the apparent fracture toughness of cracked structures. Some examples of such preloading types are warm prestressing (WPS) [1–10], shot peening, and more recently, laser peening [11–13]. One of the common contributors to the benefits of these preloads is CRS, introduced at the crack tip. Fundamental studies on the effects of the mechanical CRS on the apparent fracture toughness alone do not seem to be popular, probably because the interest of researchers with regard to the effects of these preloads has been application oriented, and the CRS in these preloads is accompanied by a microstructure change due to heat. One of the successful approaches for predicting the increase in the fracture toughness of a specimen by using a mechanically introduced CRS is a local approach proposed by Yamashita et al. [14]; the local approach [15,16] was originally developed to explain three characteristics exhibited by the cleavage fracture toughness J_c of ferritic materials in the ductile-to-brittle transition temperature (DBTT) region: (i) temperature dependence [17–20], (ii) test-specimen-size dependence [21–36], and (iii) large scatter [15,37]. These studies determined that the local approach is suitable for the prediction of increase in a specimen's fracture toughness, and the Weibull stress without and with CRS is found to be the same. This approach leads to the proposal of obtaining the Weibull stress from fracture toughness tests without CRS and the associated elastic-plastic finite element analysis (EP-FEA), and then predicting the fracture load for specimens with CRS by performing EP-FEA and by using the aforementioned Weibull stress. The local

approach eliminates the problems arising from the distributed shape of the stress. Considering that CRS distribution varies for different structures because of constraint differences, this approach is beneficial. However, owing to the statistical nature of the assumed Weibull distribution, this approach is known to require approximately 30 test data values to obtain reliable values of the Weibull parameters used for evaluating the Weibull stress [37]. Therefore, a more straightforward methodology is necessary.

Many local approaches [38–44] have been proposed to explain the three aforementioned characteristics of J_c in the DBTT region. These approaches are sophisticated, and thus have similar problems to the Weibull stress approach. In contrast, the authors' group has been developing an analytical approach that uses three-dimensional EP-FEA; this approach focuses on transferring the mean J_c between different specimen sizes [29–36] and temperatures [45]. The theoretical basis for this analytical approach is the perspective that "the size or temperature dependence of J_c is caused by the loss in the one-to-one correspondence between J and the crack-tip stress distribution." In other words, the scaled fracture stress in the DBTT region is independent of the test specimen size and temperature. Considering that fracture occurs in the DBTT region under the small-scale yielding (SSY) condition, where the EP-FEA stress distribution is enveloped by the theoretical stress intensity factor (SIF) K and Hutchinson–Rice–Rosengren (HRR) stress distributions [46], the authors developed the T-scaling method [45] to scale the crack-tip opening stress distribution under the SSY condition in a straightforward manner (i.e., by focusing on the cross point of the theoretical K and HRR stress distributions, which is named as the T-point) and successfully applied the method to predict the fracture load between different temperatures for ASTM A533B steel and JIS S55C.

In this study, fracture prediction was performed for a specimen with CRS by using the T-scaling method, and the validity of the method was confirmed for a 780-MPa-class high-strength steel and 0.45% carbon steel JIS S45C. The crack-tip opening stress distribution at the fracture load was shown to be approximately identical and close to the SSY stress distributions, regardless of the initially introduced CRS distribution. This seems to be why Weibull stress can be used to perform fracture prediction for specimens with CRS. The T-scaling method seems to have an advantage over the Weibull stress approach for predicting the point fracture load for a specimen with CRS, in that the T-scaling method can possibly complete the prediction without performing any fracture toughness tests. This is because the crack-tip opening stress at the T-point is load independent.

2. T-Scaling Method

Acknowledging that the "fracture stress for slip-induced cleavage fracture is temperature independent" [15] and assuming that the temperature dependence of J_c can be explained by the loss in the one-to-one correspondence between J and the crack-tip opening stress, in addition to considering that fracture occurs in the DBTT region under the SSY condition, where the EP-FEA stress distribution is enveloped by the theoretical K and HRR stress distributions [46], the authors developed the T-scaling method [45] to scale the crack-tip opening stress distribution under the SSY condition in a straightforward manner, as shown in Figure 1. Specifically, by assuming that J-integral under SSY J_e is equal to $(K_e)^2/E'$, where K_e is the elastic SIF and $E' = E/(1 - v^2)$ (E: Young's modulus, v: Poisson's ratio), r_T, which is the location on the x_1-axis of the cross point of the theoretical K and HRR stress distributions (σ_{22K} and σ_{22HRR}, respectively in Figure 1), named as the T-point, can be expressed in a function of K_e, as shown in Equation (1). In addition, σ_{22T}, the crack-opening stress at r_T is load-independent, as shown in Equation (2). Thus, as far as the EP-FEA σ_{22} distribution is enveloped by the two theoretical stress distributions, it is expected to be scaled for arbitrary K_e by using r_T and σ_{22T}.

$$r_T = \left[(2\pi)^{n+1} \widetilde{\sigma}_{22}(n,0)^{2(n+1)} \left(\frac{1 - v^2}{\alpha I_n} \right)^2 \right]^{\frac{-1}{n-1}} \left(\frac{K_e}{\sigma_0} \right)^2, \tag{1}$$

$$\sigma_{22T} = \sigma_0 \widetilde{\sigma}_{22}(n,0)^{\frac{n+1}{n-1}} \left[\frac{\alpha I_n}{2\pi(1 - v^2)} \right]^{\frac{1}{1-n}}, \tag{2}$$
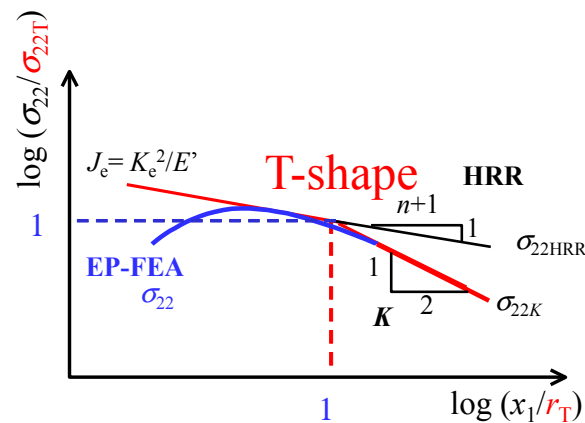
Figure 1. Explanation of the T-scaling method, which is a stress-distribution scaling method under small-scale yielding conditions [45].

Here, σ_0 and ε_0 are the reference stress and strain, respectively, α represents the parameters used in the Ramberg–Osgood power law stress–strain relationship:

$$\frac{\varepsilon}{\varepsilon_0} = \frac{\sigma}{\sigma_0} + \alpha \left(\frac{\sigma}{\sigma_0} \right)^n, \tag{3}$$

and I_n and $\widetilde{\sigma}_{22}(n, 0)$ are parameters that depend on n [47].

Next, the T-scaling method was applied to predict the fracture load, and thereby predict the fracture toughness with CRS. The aims described in the following sections are shown in a flowchart in Figure A1 in the Appendix A [45].

3. Application of T-Scaling Method to 780-MPa-Class High-Strength Steel without and with CRS

3.1. Outline of Tests to Be Reproduced

First, the applicability of the T-scaling method to the 780-MPa-class high-strength steel (HT780) was verified. The fracture toughness test results for this steel without and with CRS have been presented in a previous paper [14]. The yield and tensile strengths at room temperature were 838 and 885 MPa, respectively. The chemical compositions in weight % were C: 0.11%, Si: 0.24%, Mn: 0.84%, P: 0.0007%, S: 0.0001%, Cu: 0.16%, Cr: 0.72%, Mo: 0.41%, and V: 0.04%. Fracture toughness tests without and with CRS were performed at $-75\,^\circ\text{C}$ in accordance with the BS 7448 standard [47]. CRS was reported to be applied by preloading the specimen at $20\,^\circ\text{C}$ up to $P_{\text{pre}} = 54$ kN, and then unloading it, as illustrated in Figure 2. The reason for selecting $P_{\text{pre}} = 54$ kN was not clarified. Then, the specimen with CRS was cooled up to $-75\,^\circ\text{C}$ and loaded until fracture. A single-edged notched bend bar (SE(B)) specimen with width $W = 48$ mm, thickness $B = 24$ mm, initial crack length $a = 25.6$ mm, and support span $S = 225$ mm was used. The fracture loads P_c without and with CRS were reported to be in the range of 40–64 and 56–69 kN, respectively.

3.2. EP-FEA to Reproduce Test Results for HT780

A three-dimensional EP-FEA was performed to reproduce the fracture toughness tests for the HT780 SE(B) test specimen. Figure 3 shows the FE model for the SE(B) specimen, with the same dimensions as those of the aforementioned fracture toughness specimen. Table 1 presents a summary of the parameters of the generated mesh.
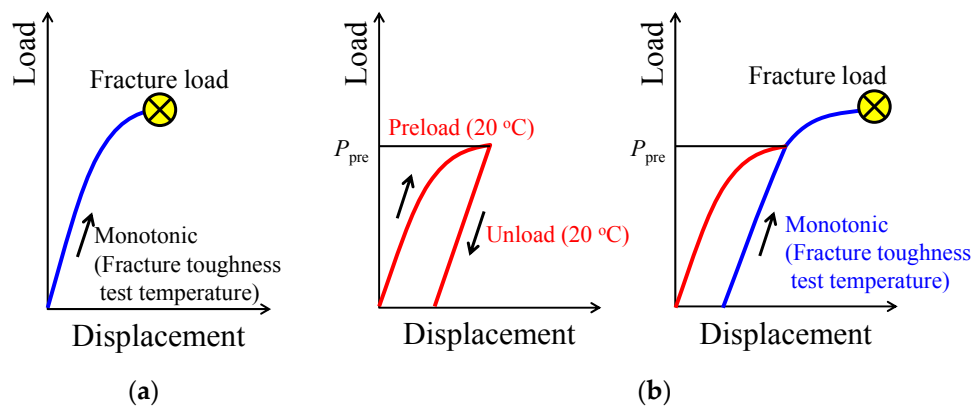
Figure 2. Loading pattern for fracture toughness tests without and with compressive residual stress (CRS): (**a**) case without CRS and (**b**) case with CRS. In case (**b**), the first figure represents the case in which CRS is applied by preloading the specimen to P_{pre} at 20 °C, and the second figure represents the case in which the specimen is loaded to fracture at the same temperature as that in case (**a**).
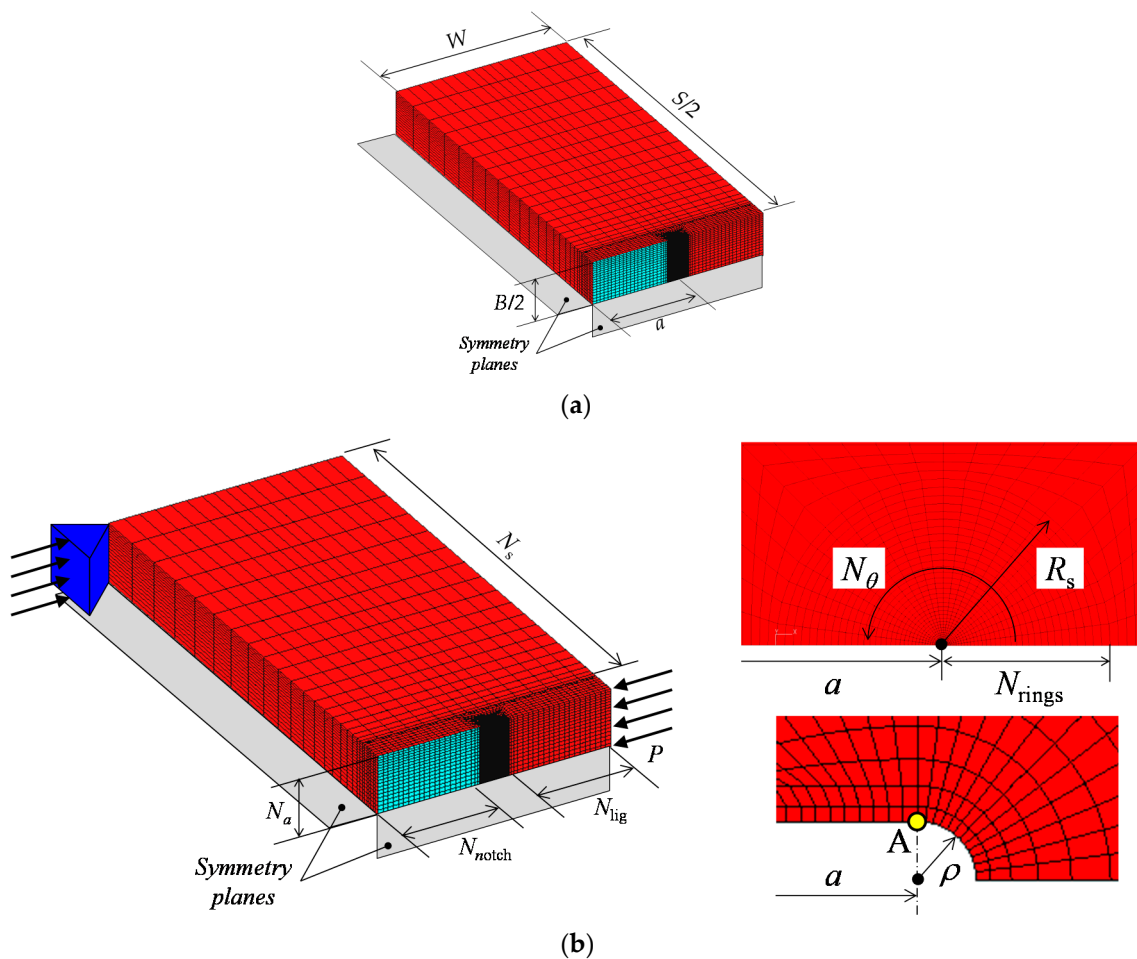

Figure 3. Definition of mesh division parameters summarized in Table 1. (**a**) Specimen geometry; (**b**) Definition of element subdivision.

Assuming that the model was symmetric, only one-fourth of the actual test specimen was modeled. The thickness of half of the test specimen was divided into 18 (N_a) spaces. The crack tube radius R_s was selected as 2.56 mm to obtain detailed information about the stress distribution for a region at least

10 times the crack-tip opening displacement (CTOD, δ_t). An initial blunted notch of radius ρ inserted at the crack tip was determined to satisfy $\delta_t/\rho > 10$ [48] at the load level near fracture, and this radius was different for the cases without and with CRS, as shown in Table 1. The CTOD was measured at node A, as shown in Figure 3b, which was the point at which the straight flank in the undeformed mesh met the curved notch surface [48]. This tube was divided into 24 (N_θ) equal spaces in the circumferential direction and 50 (N_{rings}) unequal spaces in the radial direction. For all the cases, 20-node isoparametric three-dimensional solid elements with reduced ($2 \times 2 \times 2$) Gauss integration points were employed. The total number of nodes was 156,194, and the total number of elements was 35,838. The analysis was performed using the solver WARP3D [49].

Table 1. Mesh division parameters of the finite element (FE) model of HT780 single-edged notched bend bar (SE(B)) specimens.

Model	ρ (μm)	R_s (mm)	N_a	N_{notch}	N_{lig}	N_s	N_θ	N_{rings}
Without CRS	2.5	2.56	18	18	18	20	24	50
With CRS	3.5	2.56	18	18	18	20	24	50

With regard to material behavior, the J_2 incremental theory, isotropic hardening rule, and Prandtl-Reuss flow rule were used in the analysis. Furthermore, the stress-strain curves at different temperatures were used to reproduce the tensile test results and were defined up to the value of the tensile strength. Beyond this value, the solver used a fixed stress in the analysis. The piecewise linear stress–strain curves used in the analysis are shown in Figure 4, and were discretized from the curve given in a previous paper [14]. Young's modulus $E = 206$ GPa and Poisson's ratio $\nu = 0.3$ were used for both -75 and 20 °C, according to the description in the previous paper [14]. The Ramberg–Osgood parameters (n, α, and σ_0) and the related parameters for the HRR stress distribution (I_n and $\tilde{\sigma}_{22}(n,0)$) are summarized in Table 2. As the values of I_n and $\tilde{\sigma}_{22}(n,0)$ for the case of a large n were not given in reference [50], the values for $n = 13$ were used.

The maximum value observed from the experiments was selected as the maximum load applied: 64 and 69 kN for the cases without and with CRS, respectively. The loading pattern presented in Figure 2 was reproduced for $P_{pre} = 54$ kN and fracture toughness test temperature = -75 °C. A load-controlled analysis was performed in association with the multipoint function of WARP3D so that the through-thickness displacement was uniform at the loaded nodes. The stress-strain curves used for reproducing the fracture toughness test (-75 °C) and preloading (20 °C) were different, as shown in Figure 4.
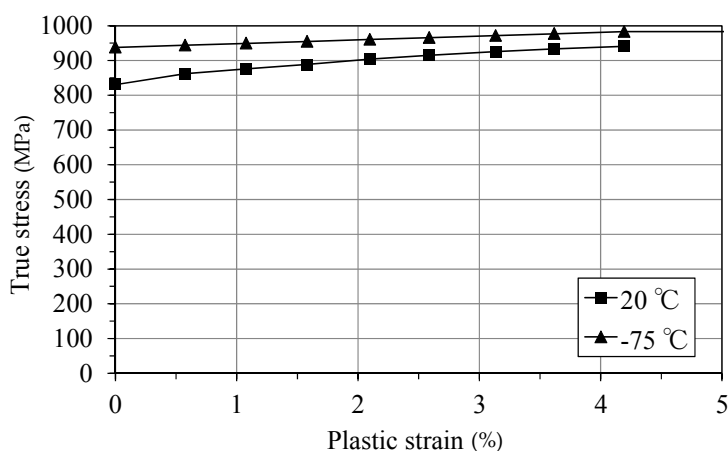

Figure 4. True stress–plastic strain curve for each temperature for HT780.

Table 2. Ramberg–Osgood parameters (σ_0, α, and n) and related Hutchinson–Rice–Rosengren (HRR) stress-distribution parameters (I_n and $\widetilde{\sigma}_{22}(n, 0)$) for HT780. Note that the values of I_n and $\widetilde{\sigma}_{22}(n, 0)$ for $n = 13$ obtained from reference [50] were used because the values of n listed in the table were very large.

T (°C)	σ_0 (MPa)	α	n	I_n	$\widetilde{\sigma}_{22}(n,0)$
20	838	2.56	19.5	4.40	2.62
−75	938	2.56	39.8	4.40	2.62

First, the EP-FEA midplane crack-opening stress distribution on the x_1-axis, denoted by σ_{22}, was normalized by the T-point stress σ_{22T} defined in Equation (2) for various loads $P/P_{\text{pre}} = 0.2$, 0.5, 0.74, 1, and 1.19 (Figure 5). In this figure, 0.74 and 1.19 represent the minimum and maximum fracture loads, respectively, observed in the experiment and divided by P_{pre}. The horizontal axis r was also normalized by the T-point location r_T defined in Equation (1). The dashed and solid lines in the figure represent σ_{22K} (K stress distribution) and $\sigma_{22\text{HRR}}$ (HRR stress distribution) on the x_1-axis, respectively, where K was calculated using the SE(B) equation as follows [17]:

$$K = \left[\frac{PS}{(BB_{\text{N}})^{1/2}W^{3/2}} \right] \frac{3(a/W)^{1/2}\left\{1.99 - (a/W)(1 - a/W)[2.15 - 3.93(a/W) + 2.7(a/W)^2]\right\}}{2[1 + 2(a/W)](1 - a/W)^{3/2}}. \quad (4)$$

The J value for the $\sigma_{22\text{HRR}}$ calculation was elastic and given as $(1 - \nu^2)K^2/E$, which was also used for defining the T-point [45].
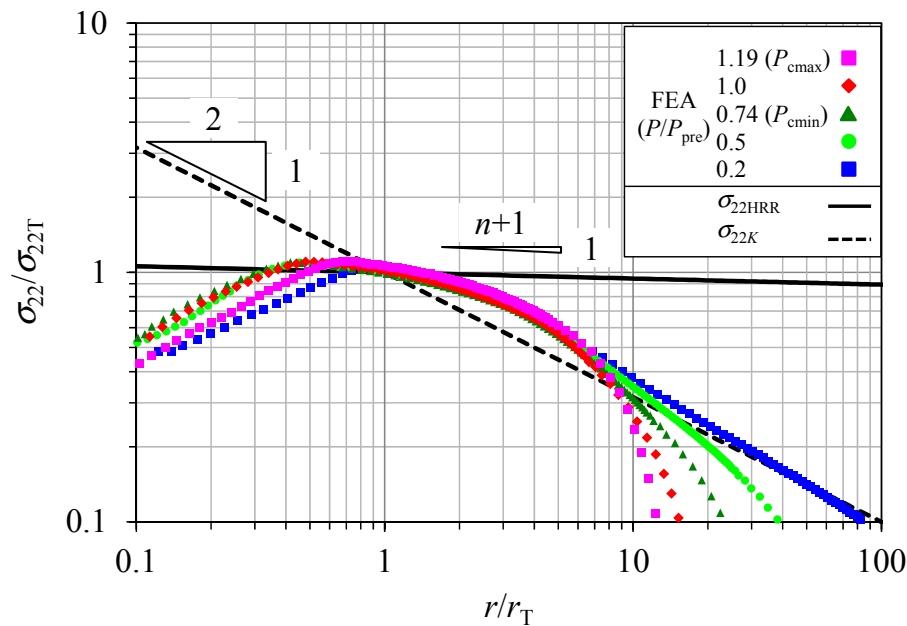

Figure 5. Crack-tip stress distribution without CRS for $P/P_{\text{pre}} = 0.2$, 0.5, 1.0, and 1.19. A significant difference was not observed in the maximum value of the σ_{22} distribution for each load level; i.e., the maximum value of σ_{22} reached the HRR stress from a low load level. Here, P_{pre} is the preload used for the case with CRS.

Figure 5 indicates that the EP-FEA σ_{22} distribution without CRS was fairly scaled from a low load up to the maximum experimental fracture load by using the aforementioned T-scaling method. The stress distribution was in the steady state and in the so-called SSY stress state.

In contrast, the EP-FEA σ_{22} distribution with CRS in the reloading procedure was considerably different, as shown in Figure 6. In this figure, the cases for P/P_{pre} = 0.5, 1, 1.04, and 1.28 are plotted. Here, 1.04 and 1.28 represent the minimum and maximum fracture loads, respectively, observed in the experiments divided by P_{pre}. The figure indicates that the stress level at a low load was very low compared to the levels in the theoretical K or HRR stress distribution, because of the initially provided CRS. However, it is interesting to note that the σ_{22} distribution was enveloped by the theoretical K and HRR stress distributions when the load was close to P/P_{pre} = 1.04, which was the minimum fracture load observed in the experiments. This finding suggested that even for the case with CRS, the specimen midplane EP-FEA σ_{22} distribution at fracture in the DBTT region was enveloped by the theoretical K and HRR stress distributions and was under the SSY condition. This led to the proposal of monitoring σ_{22} at the T-point for fracture prediction with CRS.
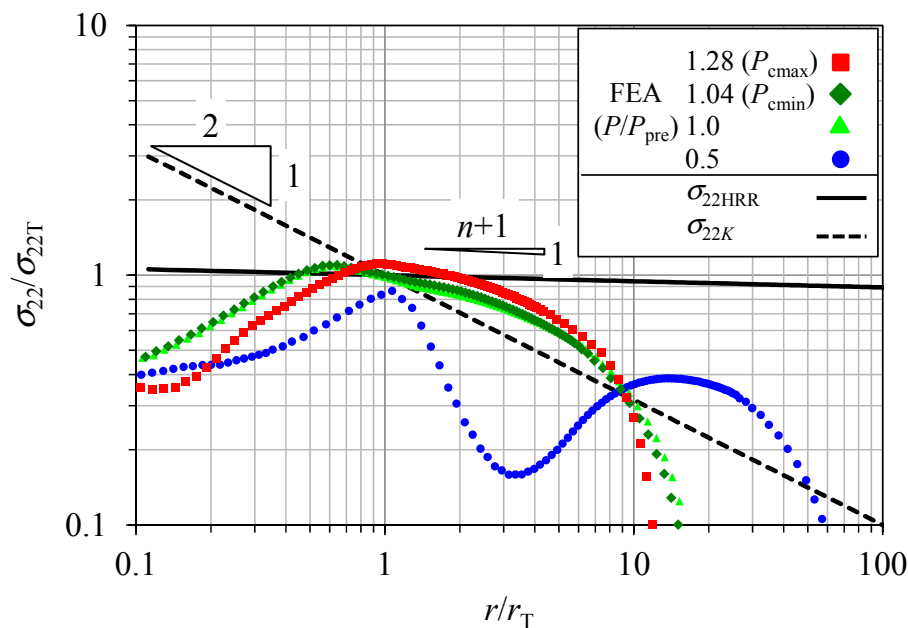

Figure 6. Midplane crack-opening stress distribution with CRS for P/P_{pre} = 0.5, 1, 1.04, and 1.28. For the load P/P_{pre} = 0.5, the effect of CRS was observed. However, for the cases of $P/P_{pre} \geq 1.0$, the σ_{22} distribution was close to that without CRS.

3.3. Proposed Method to Predict Fracture Load for Cases with CRS

The aforementioned discussion indicates that even for the case with CRS, the specimen midplane EP-FEA σ_{22} distribution at fracture in the DBTT region was enveloped by the theoretical K and HRR stress distributions and was under the SSY condition. To evaluate the confinement of the EP-FEA σ_{22} distribution to the SSY condition, the T-scaling method [45] was used. Specifically, considering that the crack-opening stress σ_{22T} (given as Equation (2)) at the theoretical T-point (i.e., r_T, which is the cross point of the K and HRR stress distributions shown in Figure 1 and given as Equation (1)) was independent of the load, the specimen midplane EP-FEA σ_{22} distribution was monitored at r_T (hereafter denoted as $\sigma_{22T\,FEA}$), as shown in Figure 7. The yellow open markers show the fracture toughness test results for the case with CRS.

Figure 7 indicates that $\sigma_{22T\,FEA}$ for the case without CRS was constant, as expected. In contrast, $\sigma_{22T\,FEA}$ for the case with CRS was significantly lower than that for the case without CRS; the $\sigma_{22T\,FEA}$ for the case with CRS showed the tendency to increase with the load, and finally became close to that of the case without CRS. As this was a numerical analysis, and considering that fracture with CRS was observed when the difference in the $\sigma_{22T\,FEA}$ value between the cases without and with CRS became less than 1%, 1% was chosen as the engineering threshold value. Based on the experience

with HT780, the fracture load prediction for the cases with CRS was proposed when the difference in $\sigma_{22T\ FEA}$ between the cases without and with CRS became less than 1%. In the following section, the validation of the proposed criterion for another material is presented.
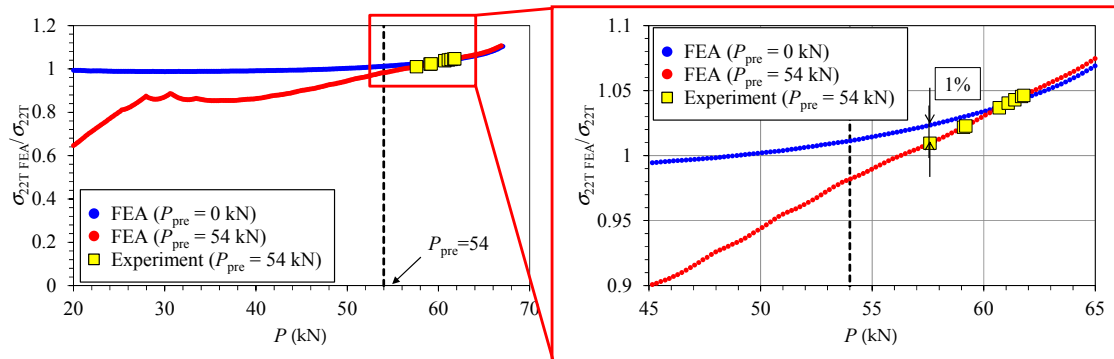

Figure 7. Comparison of relationship between normalized midplane crack-opening stress on x_1-axis $\sigma_{22T\ FEA}/\sigma_{22T}$ and load P without ($P_{pre} = 0$ kN) and with ($P_{pre} = 54$ kN) CRS for HT780. When the difference in $\sigma_{22T\ FEA}/\sigma_{22T}$ between the two cases became smaller than 1%, fracture was observed for the case with CRS.

4. Validation of Application of T-Scaling Method to Predict Fracture Load of Specimens with CRS

4.1. Material Selection

The material considered was 0.45% carbon steel JIS S45C, which was quenched at 850 °C and tempered at 550 °C. The chemical composition of the S45C specimen was summarized in Table 3.

Table 3. Chemical compositions of the S45C test specimens in weight %.

JIS S45C	C	Si	Mn	P	S	Cu	Ni	Cr
Specified	0.42–0.48	0.15–0.35	0.60–0.90	≤0.030	≤0.035	≤0.30	≤0.20	≤0.20
Check Analysis	0.47	0.17	0.64	0.009	0.004	0.02	0.02	0.02

Charpy impact tests were performed according to JIS Z 2242, and the results are shown in Figure 8. From these results, −10 and 20 °C were selected as the fracture toughness test and preloading temperatures, respectively. Next, tensile tests were performed according to JIS Z 2241. The tensile test results for the selected temperatures together with the Ramberg–Osgood parameters and related parameters of S45C are summarized in Table 4.
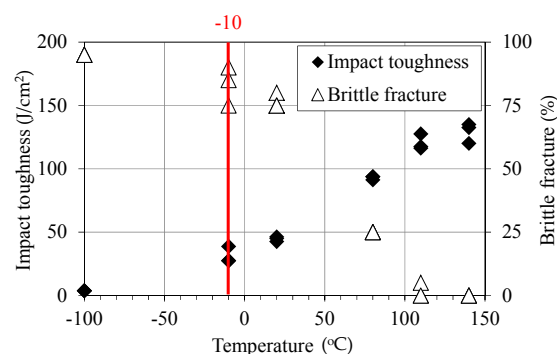

Figure 8. Charpy test results for S45C. The reference temperature of −10 °C was selected for performing fracture toughness tests in the ductile-to-brittle transition temperature (DBTT) region.

Table 4. Mechanical properties, Ramberg–Osgood parameters, and related parameters (I_n and $\tilde{\sigma}_{22}(n, 0)$) for S45C. Here, σ_{YS0} and σ_{B0} are nominal yield and tensile stresses, respectively.

T (°C)	σ_{YS0} (MPa)	σ_{B0} (MPa)	Elongation (%)	σ_0 (MPa)	α	n	I_n	$\tilde{\sigma}_{22}(n,0)$
20	467	738	22	468	2.71	4.73	5.07	2.21
−10	492	770	22	493	2.59	4.83	5.04	2.22

4.2. Fracture Toughness Tests for S45C without CRS

A fracture toughness test was performed at −10 °C by using an SE(B) specimen (width $W \times$ thickness $B = 46 \times 23$ mm) based on ASTM E1921 [17] to obtain J_c without CRS, and the fracture load for selecting P_{pre}. The dimensions of the SE(B) specimen are shown in Figure 9. Length L and support span S of the specimen were required to satisfy the conditions $L/W \geq 4.5$ and $S/W = 4.0$, and were designed as $L/W = 4.6$ and $S/W = 4.0$, where width $W = 46$ mm.
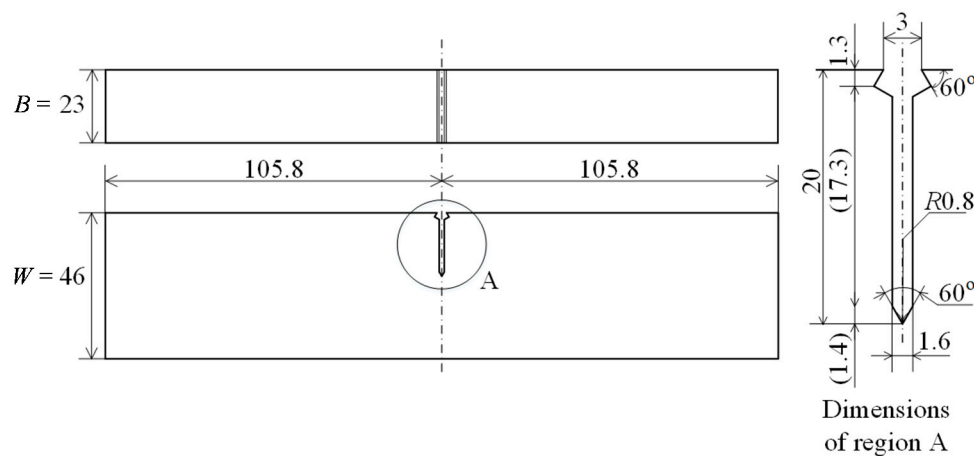

Figure 9. Dimensions of SE(B) fracture toughness test specimen used for S45C. All the dimensions are in millimeters. The support span was $4W$, where width $W = 46$ mm.

Precracking was performed using four discrete steps, which satisfied the requirement of ASTM E1921 [17] that precracking should be performed by using at least two discrete steps. Fatigue precracking was employed with loads corresponding to $K_{max} = 19.8$ and 13.8 MPam$^{1/2}$ for the 1st and last stages, respectively, which satisfied the requirement of the standard, i.e., 25 and 15 MPam$^{1/2}$. The reduction in P_{max} in each of these steps was 18%, which adhered to the suggestion of the standard that the reduction in P_{max} for any of these steps should be no greater than 20%. The ratio of the maximum force P_{max} and the minimum force P_{min}, i.e., $R = P_{min}/P_{max}$, was chosen as 0.1. The load frequency was 10 Hz. In the fracture toughness test, the loading rate was controlled within the specified range of 0.1–2.0 MPam$^{1/2}$/s and the resultant loading was in the range of 1.18–1.22 MPam$^{1/2}$/s. The test temperature was required to be held at −10 ± 3 °C for longer than $30B/25$ min, where the specimen thickness B was 23 mm, and result was −10 ± 1 °C for 45 min.

Figure 10 shows the diagram of load P versus the crack-mouth opening displacement (CMOD) V_g for the five tests. The slope of the linear part of the P–V_g diagram showed good coincidence with that obtained from the following equation, which is given in ASTM E1820 [51]. In addition, the paths of the five tests showed good reproducibility.

$$V_g = P \left\{ \frac{6S}{EWB} \left(\frac{a}{W} \right) \left[0.76 - 2.28 \left(\frac{a}{W} \right) + 3.87 \left(\frac{a}{W} \right)^2 - 2.04 \left(\frac{a}{W} \right)^3 + \frac{0.66}{(1 - a/W)^2} \right] \right\} \quad (5)$$
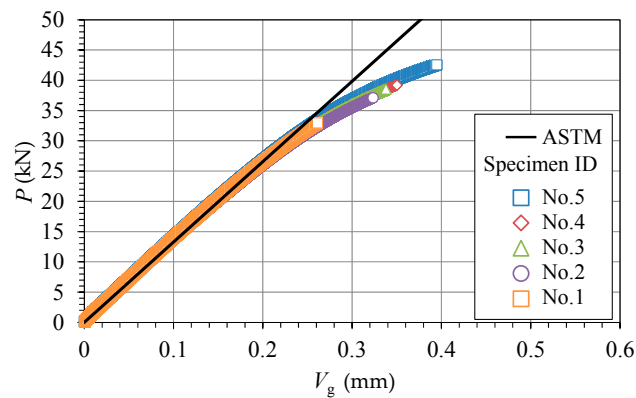
Figure 10. P–V_g diagram for case without CRS (S45C, SE(B) specimen, $W = 46$ mm, $B/W = 0.5$, $-10\,°C$). The open symbols represent the experimental results, and the solid line is calculated using Equation (5), which is given in ASTM E1820.

The test results are summarized in Table 5, where μ and Σ are the mean and standard deviation of each quantity, respectively. P_c is the fracture load, K_c is the SIF K calculated using the crack depth a at P_c, and J_c is the fracture toughness calculated using Equation (6) based on the P–V_g diagram obtained according to ASTM E1921 [17].

$$J_c = \frac{K_c^2(1 - v^2)}{E} + \frac{\eta A_P}{B(W - a)},\qquad(6)$$

where area A_P is the plastic component corresponding to the P–V_g diagram and η is a parameter defined by $\eta = 3.667 - 2.199(a/W) + 0.4376(a/W)^2$, according to ASTM E1820 [51]. $K_{Jc} = (EJ_c/(1 - v^2))^{1/2}$, where Young's modulus $E = 206$ GPa and Poisson's ratio $v = 0.3$. $M = (W - a)\,\sigma_{YS0}/J_c$, where W, a, and σ_{YS0} are the width, crack depth, and yield stress of the specimen, respectively.

Table 5. Fracture toughness test results for case without CRS (S45C, SE(B) specimen, $W = 46$ mm, $B/W = 0.5$, $-10\,°C$). Here, μ and Σ denote the mean and standard deviation of each parameter, respectively.

Specimen ID	1	2	3	4	5	μ	Σ
a/W	0.50	0.51	0.50	0.50	0.50	0.50	0.00
P_c (kN)	32.9	37.1	38.5	39.1	42.6	38.0	3.50
K_c (MPam$^{1/2}$)	71.9	81.9	83.3	85.0	91.6	82.7	7.09
J_c (N/mm)	24.8	36.0	39.3	42.0	52.1	38.8	9.87
K_{Jc} (MPam$^{1/2}$)	77.4	92.8	97.0	101	111	95.8	12.3
M	453	310	287	269	218	307	88.1

The table indicates that the standard deviation of a/W for the five specimens was 0.00, and thus the possible J_c scatter due to crack depth difference was minimized. The mean of K_{Jc} was 95.8 MPam$^{1/2}$. The standard deviation of K_{Jc} was 12.3 MPam$^{1/2}$, which was small compared to the median value of 21.2 MPam$^{1/2}$ predicted using Equation (X4. 1) in ASTM E1921 [17]. The 2% tolerance bound K_{Jc} predicted using Equation (X4. 2) in ASTM E1921 [17] was 51.9 MPam$^{1/2}$, and thus the obtained K_{Jc} values were sufficiently larger than the 2% tolerance bound value. The minimum M was 218, which satisfied the requirement of ASTM E1921 [17] of $M \geq 30$.

4.3. Selection of Load P_{pre} to Apply CRS

Preloading was planned to be applied at 20 °C according to the same procedure shown in Figure 2. The value of the preload P_{pre} was selected such that fracture would not occur during the preloading but such that the largest possible CRS would be obtained. Therefore, the minimum fracture load at

20 °C was predicted using the load obtained at −10 °C (32.9 kN, as listed in Table 4) by applying the stress-distribution scaling (SDS) method proposed in [45]. This method was developed based on the knowledge that the fracture stress for slip-induced cleavage fracture is temperature-independent [52] and can be obtained by applying the T-scaling method [45]. The SDS method can be approximated as follows:

$$\frac{P_{ci}}{P_{cr}} \approx \frac{\sigma_{0r}}{\sigma_{0i}}, \tag{7}$$

where suffixes r and *i* represent the reference and temperature of interest, respectively. P_c and σ_0 are the fracture load and Ramberg–Osgood reference stress, respectively. By using P_{cr} = 32.9 kN, σ_{0i} = 468, and σ_{0r} = 493 MPa, the minimum predicted fracture load at 20 °C was obtained as 34.7 kN. From this result, P_{pre} was selected as 33 kN, which is 95% of the predicted fracture load at 20 °C.

4.4. Prediction of Fracture Load with CRS

Next, the fracture load for the case with CRS was predicted by applying the T-scaling method. Fracture is expected to occur when the specimen midplane crack-opening stress σ_{22} on the x_1-axis at the T-point ($x_1 = r_T$ in Equation (1)) reaches the material-dependent but load-independent stress σ_{22T} given by Equation (2). Because the theoretical σ_{22T} did not coincide with EP-FEA σ_{22T}, the fracture load for the case with CRS was determined as the load when EP-FEA σ_{22} at the T-point for the cases with CRS reached 99% of that for the case without CRS, as practically shown in Figure 7.

The EP-FE model for the cases of S45C without and with CRS was generated, considering a concept similar to that for HT780, as shown in Figure 3. The details of the mesh division parameters are summarized in Table 6. The same FE model was used for the cases without and with CRS because $\delta_t/\rho > 10$ near the fracture loads with the common ρ = 1 μm. The EP-FEA procedure was the same as that used for HT780, except that the preload for S45C was set as P_{pre} = 33 kN. The stress–strain curve used for S45C is shown in Figure 11. Young's modulus E = 206 GPa and Poisson's ratio ν = 0.3 were used for both −10 and 20 °C.

Table 6. Mesh division parameters of the FE model for S45C SE(B) specimens.

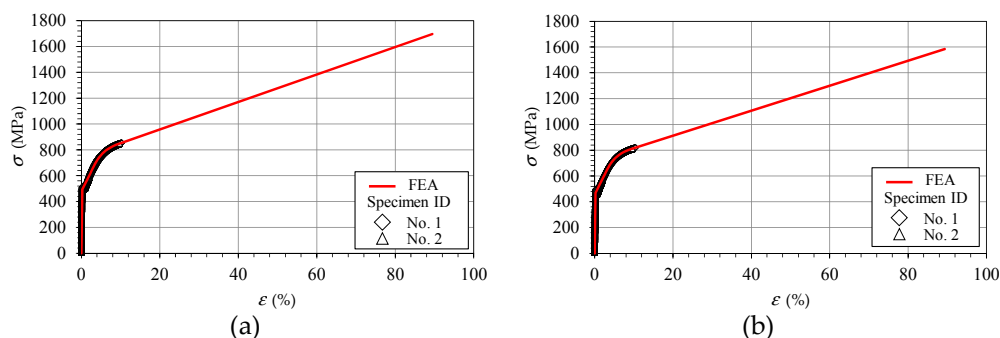| Model	ρ (μm)	R_s (mm)	N_a	N_{notch}	N_{lig}	N_s	N_θ	N_{rings}
Without CRS	1.0	2.3	18	18	18	20	24	50
With CRS	1.0	2.3	18	18	18	20	24	50

Figure 11. True stress–true strain curves for S45C used in elastic-plastic finite element analysis (EP-FEA) compared with the two tensile test results. (**a**) −10 °C, (**b**) 20 °C.

Figure 12 shows the graph of the specimen midplane EP-FEA T-point crack-opening stress $\sigma_{22T\,FEA}$ versus load P for the cases without and with CRS. The figure indicates that $\sigma_{22T\,FEA}$ with CRS reached 99% of that without CRS when the load exceeded 39.3 kN. It was expected that the fracture with CRS would occur above the predicted load P_{cT} of 39.3 kN. The following subsection presents the validation of this prediction through experiments.
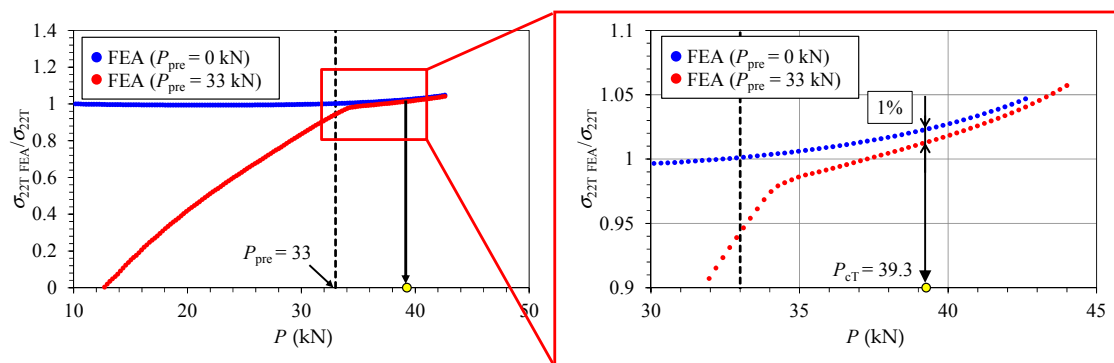
Figure 12. Comparison of relationship between normalized midplane crack-opening stress on x_1-axis $\sigma_{22T\,FEA}/\sigma_{22T}$ and load P without and with CRS for S45C. The difference in $\sigma_{22T\,FEA}/\sigma_{22T}$ between the two cases became smaller than 1% when the load reached P_{cT} = 39.3 kN for the case with CRS, and this load was used as the predicted fracture load.

4.5. Validation of Predicted Fracture Load for Specimens with CRS

To validate the proposed method to predict the fracture load for specimens with CRS, fracture toughness tests were performed at $-10\,^\circ$C according to ASTM E1921 after CRS was applied at $20\,^\circ$C by preloading the specimen up to P_{pre} = 33 kN (Figure 2). The fracture toughness test procedure is identical to that used for the aforementioned specimens without CRS (Section 4.2). Figure 13 plots the curves for load P versus the CMOD V_g for the five tests. Good reproducibility of the tests was obtained except for specimen ID 5, and the paths of specimen IDs 1–4 showed good coincidence with the FEA results. The fracture load for all the five specimens exceeded the predicted fracture load P_{cT} = 39.3 kN, and thus the proposed method was validated.
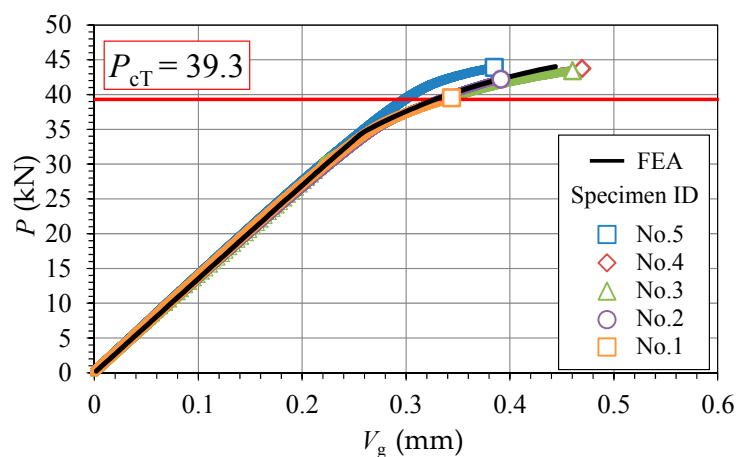

Figure 13. P–V_g diagram with CRS (S45C, SE(B) specimen, W = 46 mm, B/W = 0.5, $-10\,^\circ$C). The open symbols represent the experimental results, and the solid line is the EP-FEA result.

The detailed test results are summarized in Table 7. The minimum fracture load was 39.5 kN, which was 0.5% larger than the predicted value; thus, the prediction accuracy was good. The predicted J_c corresponding to P_{cT} was 41.5 N/mm, which was 8.2% larger than the observed minimum value; thus, the accuracy was acceptable. In summary, the fracture load prediction for the specimens with CRS as the load when the difference in $\sigma_{22T\,FEA}$ between the cases without and with CRS became less than 1% was validated for the S45C SE(B) specimen with W = 46 mm.

Table 7. Fracture toughness test results for case with CRS (S45C, SE(B) specimen, W = 46 mm, B/W = 0.5, -10 °C). Here, μ and Σ denote the mean and standard deviation of each parameter, respectively.

Specimen ID	Predicted	1	2	3	4	5	μ	Σ
a/W		0.50	0.51	0.50	0.50	0.50	0.50	0.00
P_c (kN)	39.3	39.5	42.2	43.9	43.4	43.8	42.6	1.83
K_c (MPam$^{1/2}$)	84.8	85.6	93.1	94.3	94.9	95.1	92.6	3.97
J_c (N/mm)	38.1	41.5	51.6	52.1	66.6	69.3	56.2	11.6
K_{Jc} (MPam$^{1/2}$)	93.6	98.2	110	110	125	127	114	12.0
M		272	217	218	169	163	208	44.5

5. Discussion

A method to predict the fracture load was proposed for a specimen with CRS as the load when EP-FEA σ_{22} at the T-point for the cases with CRS reached 99% of that for the cases without CRS. The proposed method was validated for a 780-MPa-class high-strength steel (HT780) and 0.45% carbon steel (JIS S45C) for predicting the minimum fracture load observed in the fracture toughness tests. As this prediction method does not refer to any of the results of the fracture toughness tests conducted for the case without CRS, it could possibly predict the minimum fracture load for specimens with CRS only from tensile test results and through EP-FEA.

In the proposed prediction method, an unwritten assumption, and thus an inherent application limit, was that the fracture occurred in the DBTT region and under the SSY condition. As mentioned by Pook [53], SSY is an ambiguous concept and has no definite criterion. One practical index is the ratio of the *J*-integral converted to *K* to the elastic *K* (i.e., K_J/K_e), which is expected to be close to unity under the SSY condition. Regarding the cases considered in this work, the corresponding index for the experimental minimum data without CRS, that is, K_{Jcmin}/K_{cmin} was 1.15 for HT780 and 1.08 for S45C. According to these results, the two considered cases seemed to satisfy the SSY condition, and thus were in the application range of the proposed prediction method. Although further investigation for other materials and other specimen types and sizes is still necessary, especially at the threshold value of 0.99, the proposed fracture load prediction method for specimens with CRS is expected to be applicable in general, as long as the SSY condition is satisfied from an engineering viewpoint.

Figure 14 compares the T-scaled midplane crack-opening stress distribution for the S45C SE(B) specimen (a) without and (b) with CRS at the fracture toughness test temperature of -10 °C. Here, P_{cmin} and P_{cmax} are the minimum and maximum fracture loads observed in experiments, respectively. P_{cT} is the predicted fracture load for the case with CRS obtained using the proposed method. The loads considered were normalized using the preload to apply the CRS, i.e., P_{pre} = 33 kN. Note that in Figure 14a, P_{cmin} without CRS coincides with P_{pre}; this might seem strange but is possible because the preload was applied at a higher temperature of 20 °C.

Figure 14a indicates that for the case without CRS, the stress distribution could be T-scaled from a low load to the maximum experimental fracture load. In contrast, Figure 14b indicates that for the case with CRS, the CRS affected the crack-tip stress distribution until the load was approximately equal to P_{pre}, and finally, the distribution was T-scaled (or, in other words, the distribution attained the SSY condition, and the EP-FEA stress distribution became enveloped by the theoretical *K* and HRR stress distributions). This finding suggests that the fracture occurred under the SSY condition without or with CRS at the test temperature of -10 °C; this supports the finding of Iwashita et al. that the Weibull stress was the same without and with CRS [14]. For the case with CRS, as fracture did not occur when the EP-FEA stress distribution did not attain the SSY stress, the increase in the fracture load and toughness due to CRS was considered to be caused by the loss in the one-to-one correspondence between *J* and the crack-tip stress distribution due to CRS at a low load.
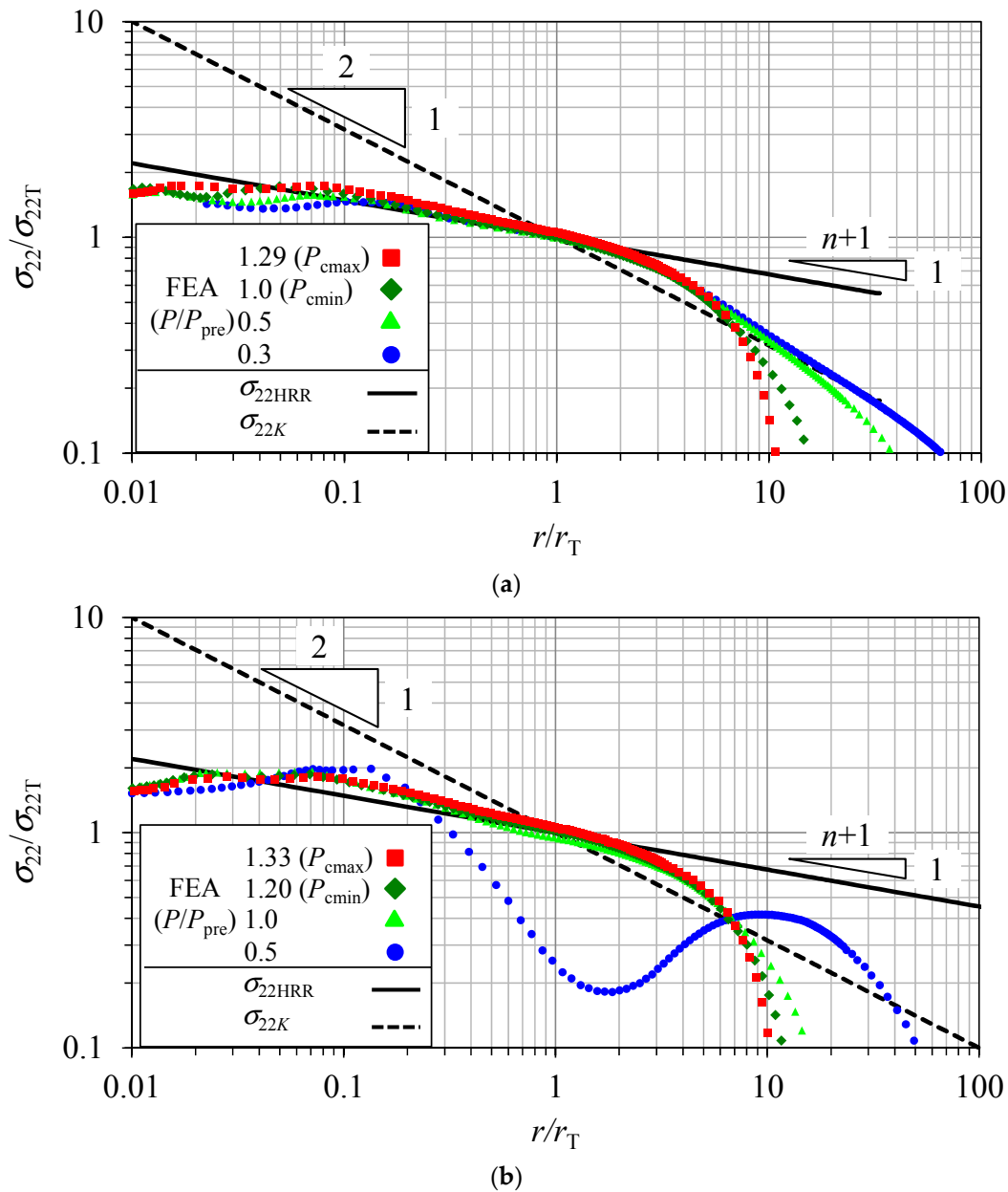
(a)

(b)

Figure 14. Comparison of T-scaled midplane crack-opening stress distribution (**a**) without and (**b**) with CRS for S45C SE(B) specimen at $-10\,^{\circ}$C. Here, P_{pre} is the preload for applying CRS, P_{cmin} and P_{cmax} are the minimum and maximum fracture loads observed in experiments, respectively. P_{cT} is the predicted fracture load obtained using the proposed method.

6. Conclusions

In this study, fracture prediction for a specimen with CRS was considered. By T-scaling the specimen's midplane crack-opening stress distribution σ_{22} on the x_1-axis, the increase in the fracture toughness resulting from the application of CRS could be because of the loss in the one-to-one correspondence between J and σ_{22}. That is, the scaled σ_{22} value for the specimen with CRS was far below the values in the K and HRR stress distributions but almost reached these theoretical stress distribution values when the load was close to the fracture load. A method to predict the fracture load was proposed for a specimen with CRS as the load when EP-FEA σ_{22} at the T-point for the cases with CRS reached 99% of that for the case without CRS. The method was validated for a 780-MPa-class high-strength steel and 0.45% carbon steel JIS S45C for predicting the minimum fracture load observed

in fracture toughness tests. For the tested cases, the experimental values of $K_{J\mathrm{cmin}}/K_{\mathrm{cmin}}$ without CRS were 1.15 for HT780 and 1.08 for S45C. This index is expected to show the closeness of the stress distribution to the SSY condition and provide an application limit for the proposed method. Future work will aim to more strictly specify this application limit for the method. As this prediction method does not refer to any of the results of the fracture toughness tests for the case without CRS, it could possibly predict the minimum fracture load for specimens with CRS only from tensile test results and through EP-FEA.

Author Contributions: Toshiyuki Meshii conceived and designed the analysis and experiments; Kenichi Ishihara performed the EP-FEA; Toshiyuki Meshii and Kenichi Ishihara analyzed the data; and Toshiyuki Meshii wrote the paper.

Conflicts of Interest: The authors declare no conflict of interest.

Nomenclature

B	Test specimen thickness
E	Young's modulus
J	J-integral
J_c	Fracture toughness obtained from experimental results
K_c	Stress intensity factor corresponding to fracture load P_c
K_e	Elastic stress intensity factor
K_{Jc}	Fracture toughness expressed in terms of K ($=(EJ_c/(1-\nu^2))^{1/2}$)
P_c	Fracture load
P_{pre}	Preload for applying compressive residual stress
V_g	Crack-mouth opening displacement
W	Specimen width
α, n	Parameters of Ramberg–Osgood power law
a	Crack depth
ε_0	Reference strain for Ramberg–Osgood power law
$I_n, \widetilde{\sigma}_{22}(n,0)$	Parameters depending on n and θ for HRR stress solution
ν	Poisson's ratio
r_{T}	Intersection point between K and HRR stress distributions (T-point)
δ_{t}	Crack-tip opening displacement
σ_{ij}	Stress components (i, j = 1, 2, 3)
σ_0	Reference stress for Ramberg–Osgood power law
$\sigma_{22\mathrm{HRR}}$	Stress of J-dominated region described as HRR stress distribution
σ_{22K}	Stress of K-dominated region described as K stress distribution
$\sigma_{22\mathrm{T}}$	Crack-opening stress σ_{22} at $r = r_{\mathrm{T}}$

Abbreviations

ASTM	American Society for Testing and Materials
BS	British Standard
CRS	Compressive residual stress
CTOD	Crack-tip opening displacement
DBTT	Ductile-to-brittle transition temperature
EP-FEA	Elastic–plastic finite element analysis
HRR	Hutchinson–Rice–Rosengren
HT780	780-MPa-class high-strength steel
JIS	Japan Industrial Standard
SE(B)	Single-edge notched bend bar
SIF	Stress-intensity factor
SSY	Small-scale yielding
T-point	Location where σ_{22HRR} and σ_{22K} intersect on x_1-axis

Appendix

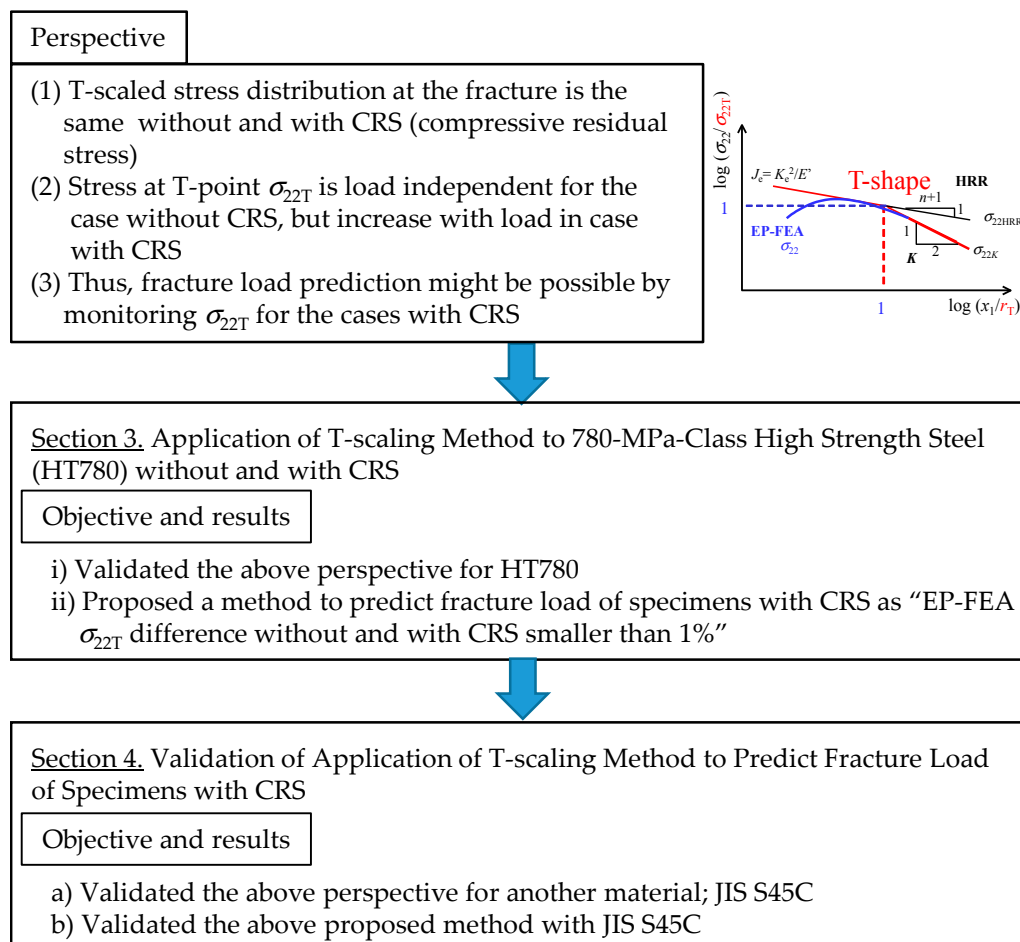The constitution of this manuscript is shown in Figure A1.

Figure A1. Constitution of this manuscript.

References

1. Chell, G.G.; Haigh, J.R.; Vitek, V. A theory of warm prestressing: Experimental validation and the implications for elastic plastic failure criteria. *Int. J. Fract.* **1981**, *17*, 61–81. [CrossRef]

2.   Curry, D.A. A micromechanistic approach to the warm pre-stressing of ferritic steels. *Int. J. Fract.* **1981**, *17*, 335–343. [CrossRef]

3.   Reed, P.A.S.; Knott, J.F. Investigation of the role of residual stresses in the warm prestress (WPS) effect. Part I—Experimental. *Fatigue Fract. Eng. Mater. Struct.* **1996**, *19*, 485–500. [CrossRef]

4.   Pokrovsky, V.V.; Troshchenko, V.T.; Kopcmsky, G.A.; Kaplunenko, V.G.; Fiodorov, V.G.; Dragunov, Y.G. The influence of plastic prestraining on brittle fracture resistance of metallic materials with cracks. *Fatigue Fract. Eng. Mater. Struct.* **1995**, *18*, 731–746. [CrossRef]

5.   Okamura, H.; Yagawa, G.; Hidaka, T.; Urabe, Y.; Satoh, M.; Tomimatsu, M.; Koyama, K.; Iida, M. Further experimental verification of warm prestressing effect under pressurized thermal shock (PTS). *J. Press. Vessel Technol.* **1996**, *118*, 174–180. [CrossRef]

6.   Cheng, J.; Noble, F.W. The warm prestressing effect in steels undergoing intergranular fracture. *Fatigue Fract. Eng. Mater. Struct.* **1997**, *20*, 1399–1411. [CrossRef]

7.   Smith, D.J.; Hadidimoud, S.; Fowler, H. The effects of warm pre-stressing on cleavage fracture. Part 1: Evaluation of experiments. *Eng. Fract. Mech.* **2004**, *71*, 2015–2032. [CrossRef]

8.   Jacquemoud, C.; Marie, S.; Nédélec, M. Evaluation of the active plasticity hypothesis as a relevant justification of the warm pre stressing effect. *Eng. Fract. Mech.* **2013**, *104*, 16–28. [CrossRef]

9.   Yuritzinn, T.; Ferry, L.; Chapuliot, S.; Moinereau, D.; Dahl, A.; Gilles, P. Warm pre-stressing tests on specimens with semi-elliptical cracks and analysis of the results. *Eng. Fract. Mech.* **2010**, *77*, 71–83. [CrossRef]

10.   Van Gelderen, D.G.A.; Rosahl, K.; Booker, J.D.; Smith, D.J. Monte Carlo simulations of the effects of warm pre-stress on the scatter in fracture toughness. *Eng. Fract. Mech.* **2015**, *134*, 124–147. [CrossRef]

11.   Rubio-González, C.; Ocaña, J.L.; Gomez-Rosas, G.; Molpeceres, C.; Paredes, M.; Banderas, A.; Porro, J.; Morales, M. Effect of laser shock processing on fatigue crack growth and fracture toughness of 6061-T6 aluminum alloy. *Mater. Sci. Eng. A* **2004**, *386*, 291–295. [CrossRef]

12.   Kalentics, N.; Boillat, E.; Peyre, P.; Ćirić-Kostić, S.; Bogojević, N.; Logé, R.E. Tailoring residual stress profile of selective laser melted parts by laser shock peening. *Addit. Manuf.* **2017**, *16*, 90–97. [CrossRef]

13.   Huang, S.; Wang, Z.; Sheng, J.; Agyenim-Boateng, E.; Liu, M.; Yang, X.; Zhou, J. Residual stress distribution and microstructure evolution of AA 6061-T6 treated by warm laser peening. *Metals* **2016**, *6*, 292. [CrossRef]

14.   Yamashita, Y.; Sakano, K.; Minami, F.; Onozuka, M. Local approach to brittle fracture under residual stress field-Evaluation of effect of compressive residual stress caused by pre-loading. *J. Soc. Nav. Archit. Jpn.* **1999**, *186*, 455–463. [CrossRef]

15.   Beremin, F.M.; Pineau, A.; Mudry, F.; Devaux, J.C.; D'Escatha, Y.; Ledermann, P. A local criterion for cleavage fracture of a nuclear pressure vessel steel. *Metall. Mater. Trans. A* **1983**, *14*, 2277–2287. [CrossRef]

16.   Mudry, F. A local approach to cleavage fracture. *Nucl. Eng. Des.* **1987**, *105*, 65–76. [CrossRef]

17.   American Society for Testing and Materials (ASTM). E1921-10 standard test method for determination of reference temperature, T_o, for ferritic steels in the transition range. In *Annual Book of ASTM Standards*; American Society for Testing and Materials: Philadelphia, PA, USA, 2010; Volume 3.01. [CrossRef]

18.   Wallin, K. *Master Curve Analysis of Ductile to Brittle Transition Region Fracture Toughness Round Robin Data. The "EURO" Fracture Toughness Curve*; Technical Research Centre of Finland: Espoo, Finland, 1998; p. 58, ISBN 951-38-5345-4.

19.   Wallin, K. Irradiation damage effects on the fracture toughness transition curve shape for reactor pressure vessel steels. *Int. J. Press. Vessel. Pip.* **1993**, *55*, 61–79. [CrossRef]

20.   Wallin, K. Master curve analysis of the "Euro" fracture toughness dataset. *Eng. Fract. Mech.* **2002**, *69*, 451–481. [CrossRef]

21.   Wallin, K. The size effect in K_{IC} results. *Eng. Fract. Mech.* **1985**, *22*, 149–163. [CrossRef]

22.   Dodds, R.H.; Anderson, T.L.; Kirk, M.T. A framework to correlate a/W ratio effects on elastic-plastic fracture toughness (J_c). *Int. J. Fract.* **1991**, *48*, 1–22. [CrossRef]

23.   Kirk, M.T.; Dodds, R.H.; Anderson, T.L. An approximate technique for predicting size effects on cleavage fracture toughness (J_c) using the elastic T stress. In *STP 1207, Fracture Mechanics: 24th Volume*; Landes, J.D., McCabe, D.E., Boulet, J.A.M., Eds.; American Society for Testing and Materials: Philadelphia, PA, USA, 1994; Volume STP 1207, pp. 62–86. [CrossRef]

24.   Matvienko, Y.G.; Nikishkov, G.P. Two-parameter J-A concept in connection with crack-tip constraint. *Theor. Appl. Fract. Mech.* **2017**, *92*, 306–317. [CrossRef]

25.　Nevalainen, M.; Dodds, R.H. Numerical investigation of 3-D constraint effects on brittle fracture in SE(B) and C(T) specimens. *Int. J. Fract.* **1995**, *74*, 131–161. [CrossRef]

26.　Theiss, T.J.; Bryson, J.W. Influence of crack depth on the fracture toughness of reactor pressure vessel steel. In *STP 1171, Constraint Effects in Fracture*; Hackett, E.M., Ed.; American Society for Testing and Materials: Philadelphia, PA, USA, 1993; Volume STP 1171, pp. 104–119. [CrossRef]

27.　Sumpter, J.D.G. An experimental investigation of the *T* stress approach. In *STP 1171, Constraint Effects in Fracture*; Hackett, E.M., Schwalbe, K.-H., Dodds, R.H., Eds.; American Society for Testing and Materials: Philadelphia, PA, USA, 1993; Volume STP 1171, pp. 495–502. [CrossRef]

28.　Rathbun, H.J.; Odette, G.R.; He, M.Y.; Yamamoto, T. Influence of statistical and constraint loss size effects on cleavage fracture toughness in the transition—A model based analysis. *Eng. Fract. Mech.* **2006**, *73*, 2723–2747. [CrossRef]

29.　Meshii, T.; Tanaka, T. Experimental T_{33}-stress formulation of test specimen thickness effect on fracture toughness in the transition temperature region. *Eng. Fract. Mech.* **2010**, *77*, 867–877. [CrossRef]

30.　Meshii, T.; Tanaka, T.; Lu, K. *T*-stress solutions for a semi-elliptical axial surface crack in a cylinder subjected to mode-I non-uniform stress distributions. *Eng. Fract. Mech.* **2010**, *77*, 2467–2478. [CrossRef]

31.　Meshii, T.; Yamaguchi, T. Applicability of the modified Ritchie–Knott–Rice failure criterion to transfer fracture toughness J_c of reactor pressure vessel steel using specimens of different thicknesses—Possibility of deterministic approach to transfer the minimum J_c for specified specimen thicknesses. *Theor. Appl. Fract. Mech.* **2016**, *85*, 328–344. [CrossRef]

32.　Lu, K.; Meshii, T. A systematic investigation of *T*-stresses for a variety of center-cracked tension specimens. *Theor. Appl. Fract. Mech.* **2015**, *77*, 74–81. [CrossRef]

33.　Lu, K.; Meshii, T. Application of T_{33}-stress to predict the lower bound fracture toughness for increasing the test specimen thickness in the transition temperature region. *Adv. Mater. Sci. Eng.* **2014**, *2014*, 1–8. [CrossRef]

34.　Lu, K.; Meshii, T. Three-dimensional *T*-stresses for three-point-bend specimens with large thickness variation. *Eng. Fract. Mech.* **2014**, *116*, 197–203. [CrossRef]

35.　Meshii, T.; Lu, K.; Takamura, R. A failure criterion to explain the test specimen thickness effect on fracture toughness in the transition temperature region. *Eng. Fract. Mech.* **2013**, *104*, 184–197. [CrossRef]

36.　Meshii, T.; Yamaguchi, T.; Higashino, Y. Applicability of the modified Ritchie-Knott-Rice failure criterion to examine the feasibility of miniaturized Charpy type SE(B) specimens. *Adv. Mater. Sci. Eng.* **2016**, *2016*, 3728035. [CrossRef]

37.　Khalili, A.; Kromp, K. Statistical properties of Weibull estimators. *J. Mater. Sci.* **1991**, *26*, 6741–6752. [CrossRef]

38.　Sherry, A.H.; Lidbury, D.P.G.; Bass, B.R.; Williams, P.T. Developments in local approach methodology with application to the analysis/re-analysis of the NESC-1 PTS benchmark experiment. *Int. J. Press. Vessel. Pip.* **2001**, *78*, 237–249. [CrossRef]

39.　Petti, J.P.; Dodds, R.H. Calibration of the Weibull stress scale parameter, σ_u, using the master curve. *Eng. Fract. Mech.* **2005**, *72*, 91–120. [CrossRef]

40.　Wasiluk, B.; Petti, J.P.; Dodds, J.R.H. Temperature dependence of Weibull stress parameters: Studies using the Euro-material. *Eng. Fract. Mech.* **2006**, *73*, 1046–1069. [CrossRef]

41.　Burstow, M.C.; Beardsmore, D.W.; Howard, I.C.; Lidbury, D.P.G. The prediction of constraint-dependent R6 failure assessment lines for a pressure vessel steel via micro-mechanical modelling of fracture. *Int. J. Press. Vessel. Pip.* **2003**, *80*, 775–785. [CrossRef]

42.　Qian, G.; González-Albuixech, V.F.; Niffenegger, M. Calibration of Beremin model with the master curve. *Eng. Fract. Mech.* **2015**, *136*, 15–25. [CrossRef]

43.　Minami, F.; Brückner-Foit, A.; Munz, D.; Trolldenier, B. Estimation procedure for the Weibull parameters used in the local approach. *Int. J. Fract.* **1992**, *54*, 197–210. [CrossRef]

44.　Dodds, R.H.; Shih, C.F.; Anderson, T.L. Continuum and micromechanics treatment of constraint in fracture. *Int. J. Fract.* **1993**, *64*, 101–133. [CrossRef]

45.　Ishihara, K.; Hamada, T.; Meshii, T. T-scaling method for stress distribution scaling under small-scale yielding and its application to the prediction of fracture toughness temperature dependence. *Theor. Appl. Fract. Mech.* **2017**, *90*, 182–192. [CrossRef]

46.　Anderson, T.L. *Fracture Mechanics*, 3rd ed.; CRC Press: Boca Raton, FL, USA, 2005; ISBN 9781420058215.

47.　*BS 7448-1:1991 Fracture Mechanics Toughness Tests. Method for Determination of KIc, Critical CTOD and Critical J Values of Metallic Materials*; BSI Group: London, UK, 1991; Volume BS7448, ISBN 0-580-20037-X.

48. McMeeking, R.M. Finite deformation analysis of crack-tip opening in elastic-plastic materials and implications for fracture. *J. Mech. Phys. Solids* **1977**, *25*, 357–381. [CrossRef]

49. Healy, B.; Gullerud, A.; Koppenhoefer, A.R.; RoyChowdhury, S.; Petti, J.; Walters, M.; Bichon, B.; Cochran, K.; Carlyle, A.; Sobotka, J.; et al. *WARP3D—Release 17.5.9 Manual*; University of Illinois at Urbana-Champaign: Champaign, IL, USA, 2015.

50. Hutchinson, J.W. Singular behaviour at the end of a tensile crack in a hardening material. *J. Mech. Phys. Solids* **1968**, *16*, 13–31. [CrossRef]

51. American Society for Testing and Materials (ASTM). E1820-06a Standard test method for measurement of fracture toughness. In *Annual Book of ASTM Standards*; ASTM: Philadelphia, PA, USA, 2006; Volume 3.01. [CrossRef]

52. Ritchie, R.O.; Knott, J.F.; Rice, J.R. On the relationship between critical tensile stress and fracture toughness in mild steel. *J. Mech. Phys. Solids* **1973**, *21*, 395–410. [CrossRef]

53. Pook, L.P. A 50-year retrospective review of three-dimensional effects at cracks and sharp notches. *Fatigue Fract. Eng. Mater. Struct.* **2013**, *36*, 699–723. [CrossRef]